Transformation of CeO_2 Nanoparticles into Atomically Dispersed Ce Cations Leads to Enhanced Reactivity for Automotive Emissions Control

Dong Jiang,[1] Hien N. Pham,[2] Yixiao Li,[1] Yubing Lu,[3] Wenda Hu,[1] Gang Wan,[4] Chaochao Dun,[3] Junrui Li,[1] Carlos E. García-Vargas,[1] Yipeng Sun,[5] Anthony Savoy,[1] Weixin Huang,[1] Rui Zhang,[1] Andrew T. DeLaRiva,[2] Soyoung Kim,[3] Xiang Li,[6] Jeffrey J. Urban,[3] Junko Yano,[3] Kelly Shelly,[7] Chengjun Sun,[7] Konstantin Khivantsev,[8] Christopher J. Tassone,[6] Jianzhi Hu,[8] Janos Szanyi,[8] Abhaya K. Datye,[2]* Yong Wang[1,8]*

Affiliations:

[1] The Gene and Linda Voiland School of Chemical Engineering and Bioengineering, Washington State University, Pullman, WA 99164, USA.

[2] Department of Chemical and Biological Engineering and Center for Micro-Engineered Materials, University of New Mexico, Albuquerque, NM 87131, USA.

[3] Lawrence Berkeley National Laboratory, Berkeley, CA 94720, USA.

[4] Department of Mechanical Engineering, Stanford University, Stanford, CA 94305

[5] Environmental Catalysis, BASF Corporation, Iselin, NJ, USA

[6] SLAC National Accelerator Laboratory, Menlo Park, CA 94025, USA.

[7] Advanced Photon Source, Argonne National Laboratory, Lemont, IL 60439, USA.

[8] Institute for Integrated Catalysis, Pacific Northwest National Laboratory, Richland, WA 99354, USA.

*Corresponding author. Email: yong.wang@pnnl.gov, datye@unm.edu

Abstract: Nanosized cerium oxide has been extensively used as the oxygen storage component in automotive emission control systems. Here, we demonstrate the controllable transformation of cerium oxide nanoparticles into isolated cerium cations on γ-Al_2O_3 via reductive atom trapping, achieving over half-monolayer coverage. Dispersed Ce_1 anchored by surface penta- and octa-coordinated Al sites shows outstanding thermal stability. Supported Rh_1 single atoms neighbored by Ce_1 are much superior to Rh_1 on bare Al_2O_3 or CeO_2 in catalyzing NO reduction, exhibiting an increased activity by one order of magnitude at 250 °C. Dispersed Ce_1 on Al_2O_3 shows greatly enhanced oxygen transfer capability and substantially modifies the reaction mechanism to a Rh_1-Ce_1 dual-site mechanism with a much-lowered barrier. Similar enhancements are also seen with Ce_1-promoted Pt nanoparticles for CO and hydrocarbon oxidation.

One-Sentence Summary: Dispersed Ce cations on Al_2O_3 surface via reductive atom trapping greatly promote catalytic reactions over supported metals.

Ceria (CeO_2) with a face-centered cubic (FCC) fluorite structure is technologically important due to its wide applications in catalysis, gas sensors, ceramic fuel cells, water splitting, and many others (*1*). As a structural/electronic promoter, nanosized ceria has attracted intense interest in catalyzing chemical reactions, such as three-way catalysis (TWC), water-gas shift (WGS) reaction, and photocatalytic and electrochemical reactions (*2-5*). Such versatility originates from facile transformations of the cerium oxidation state between Ce^{4+} and Ce^{3+} in redox environments, accompanied by release, storage, and transport of lattice oxygen (*6*). Great progress has been made in tailoring the redox properties of ceria via different strategies, including heteroatom doping, facet regulation, and defect engineering (*7-9*). Recently, surface trapping of metal single atoms was found to enhance the reducibility and thermal stability of ceria (*10-12*). Despite great success in understanding crystalline ceria, knowledge of spatially isolated cerium atoms in heterogeneous catalysis is very limited, in contrast to homogeneous reactions over cerium complexes (*13, 14*).

With advances in material synthesis and characterization on an atomic scale, single-atom catalysts (SACs) with isolated metal centers have attracted great interest in bridging the material gap between homogeneous and heterogeneous catalysts (*15-18*). Atomically dispersed Ce_1 has been occasionally observed on oxides and was suspected to influence catalytic properties (*19-24*). For example, highly dispersed CeO_x species were deposited onto Al_2O_3 via a pulsed arc-plasma process (*19*). Recently, we also observed increased populations of dispersed CeO_x in commercial CeO_2-Al_2O_3 oxides after running emission control reactions under harsh conditions (*25*). The loading of Ce_1 is typically low (< 1 wt %), beyond which crystalline CeO_2 nanoparticles (NPs) form (*19, 22, 23*). Moreover, the location of dispersed Ce_1 and its interaction with the support and active centers are largely unknown. Due to the lack of precise control on Ce_1 dispersion over a wide range of loadings, key information is missing in linking the structure and catalytic property of Ce_1 promoters in heterogeneous catalysis.

Here, we present a controllable transformation of ceria NPs into isolated cerium cations (Ce_1) on the surface of non-reducible oxide supports like Al_2O_3 and SiO_2. Over half-monolayer Ce_1 coverage on Al_2O_3 can be achieved at ~ 10 wt % ceria loading via reductive atom trapping, above which isolated Ce_1 and crystalline CeO_2 coexist. The dispersed Ce_1 cations are anchored by surface penta- and octa-coordinated Al sites and are thermally stable in air up to 500 °C. With precise control of CeO_2 dispersion, single-atom $Rh_1/Ce_1/Al_2O_3$ catalysts with well-defined hierarchical structures are constructed for catalytic NO reduction by CO. Isolated Rh_1 neighbored by Ce_1 exhibits greatly enhanced NO reduction activity, nearly one order of magnitude higher (125 °C) than Rh_1 on bare Al_2O_3. Dispersed Ce_1 on Al_2O_3 exhibits much superior oxygen transfer capability compared to crystalline CeO_2. Structure-property relationships of Ce_1 promoter were elucidated. Ce_1 neighboring of Rh_1 substantially modifies the reaction mechanism between NO and CO, rendering a greatly lowered energy barrier.

Ceria/alumina mixed oxides have been widely employed in automotive emissions control, integrating the outstanding redox property of CeO_2 as a catalytic promoter with the superior poisoning and sintering resistance of Al_2O_3 as a support (*26-28*). In this work, different amounts of Ce (III) nitrate (0-10 wt % CeO_2 basis) were deposited on the surface of a commercial γ-Al_2O_3 (~ 130 m^2/g) via incipient wetness impregnation followed by calcination in air at 800 °C. As-obtained CeO_2/Al_2O_3 is termed as CAx with x indicating the content (wt %) of CeO_2. Intense X-ray diffractions of crystalline CeO_2 with a cubic fluorite structure were evident once CeO_2 loading is > 2 wt %, e.g., CA04 (fig. S1). Introduction of CeO_2 with a higher sintering tendency resulted in

slightly decreased surface areas of final CAx (fig. S2), e.g., ~ 120 m^2/g for CA10. Absence of CeO_2 diffractions in CA02 should be due to the low CeO_2 content as well as the high dispersion.

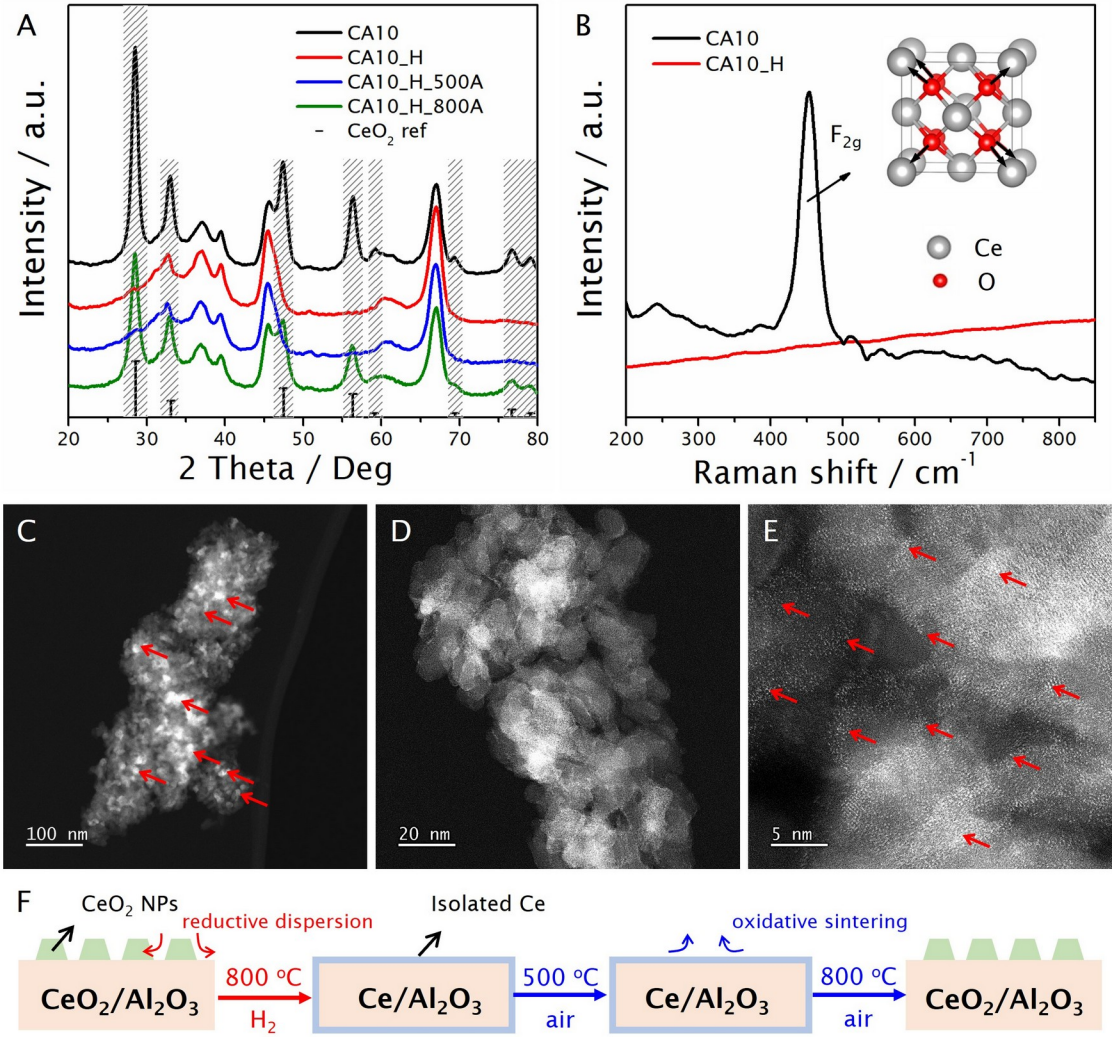

Fig. 1. Reductive dispersion of ceria NPs into isolated cerium atoms on γ-Al_2O_3. (**A**) X-ray diffraction (XRD) patterns of the 10 wt % CeO_2/Al_2O_3 after calcination in air (CA10), high-temperature (800 °C) reduction in 10 % H_2 (CA10_H), and subsequent air calcination at 500 °C (_500A) and 800 °C (_800A). (**B**) Raman (532 nm) spectra of the air-calcined CA10 and high-temperature reduced CA10_H. Fluorite structure and the F_{2g} vibration mode are shown in the inset. (**C**) AC-STEM image of CA10 showing the presence of CeO_2 NPs. (**D**) – (**E**) AC-STEM images of CA10_H showing the absence of nanoparticles and the abundant presence of isolated Ce_1. (**F**) Schematic of high-temperature reductive dispersion and oxidative sintering of Ce_1.

Interestingly, all CeO_2 diffraction peaks in CAx (e.g., CA10) diminished after being reduced in 10 % H_2 reduction at 800 °C (CA10_H) while the crystalline structure of γ-Al_2O_3 remained unchanged (Fig. 1A). The absence of CeO_2 diffractions suggests either the CeO_2 dispersion into isolated Ce_1 or the amorphization of NPs. The latter can be excluded since no clusters/NPs were visible via TEM (shown later) and air calcination at 500 °C (enough for ceria crystallization) did not recrystallize it (Fig. 1A). The reductive dispersion of CeO_2 on Al_2O_3 was also suggested by

disappearance of Raman active F_{2g} mode in CA10_H, originating from a symmetric breathing vibration of tetrahedrally-coordinated oxygen ions (Fig. 1B). The similar phenomenon was also reported by Shyu et al. who ascribed change in the Raman spectrum to the formation of $CeAlO_3$ (*29*), which we did not detect via XRD/TEM. The structural changes were further confirmed by aberration-corrected scanning transmission electron microscopy (AC-STEM) investigation. CA10 mostly contains CeO_2 NPs on Al_2O_3 (Fig. 1C), although a small amount of singly dispersed Ce_1 (< 1 wt %) was also observed (fig. S3), consistent with previous reports on Al_2O_3 and TiO_2 (*20, 22*). Notably, only isolated Ce_1 was identified after H_2 reduction, densely covering γ-Al_2O_3 (Figs. 1D and 1E).

Based on above characterization, the reductive dispersion of CeO_2 can be concluded, driven by high-temperature CeO_2 amorphization, followed by spreading and anchoring of reduced Ce_1 species on the Al_2O_3 surface (Fig. 1F). Sublimation of nanosized CeO_2 has also been recently noticed using TEM upon prolonged exposure to a focused electron beam or under vacuum at high temperatures, both being reducing conditions (*30*). Dispersed Ce_1 is stabilized by the support to a great extent and sinters only after 800 °C air calcination (Figs. 1A and 1F). The as-formed Ce_1/Al_2O_3 structure differs from crystalline $CeAlO_3$ polymorphs generated via solid-state reaction between CeO_2 and Al_2O_3 at much higher temperatures, e.g., > 900 °C (*31*). The upper limit for dispersing ceria was found to be ~ 10 wt % CeO_2 (i.e., CA10) for the used Al_2O_3 and crystalline CeO_2 was detected by XRD beyond this threshold for anchoring isolated Ce_1 atoms (fig. S4). This corresponds to over half-monolayer coverage of Ce_1 on Al_2O_3, giving a surface density of ~ 3.5 Ce/nm^2 (fig. S5) (*21*). Such Ce_1 dispersion phenomenon was also observed on other non-reducible supports like SiO_2 (fig. S6). An intimate contact between CeO_2 and Al_2O_3 is indispensable for achieving such Ce_1 dispersion, which cannot happen through the vapor phase in the case of the physical mixture of CeO_2 and Al_2O_3 (fig. S7).

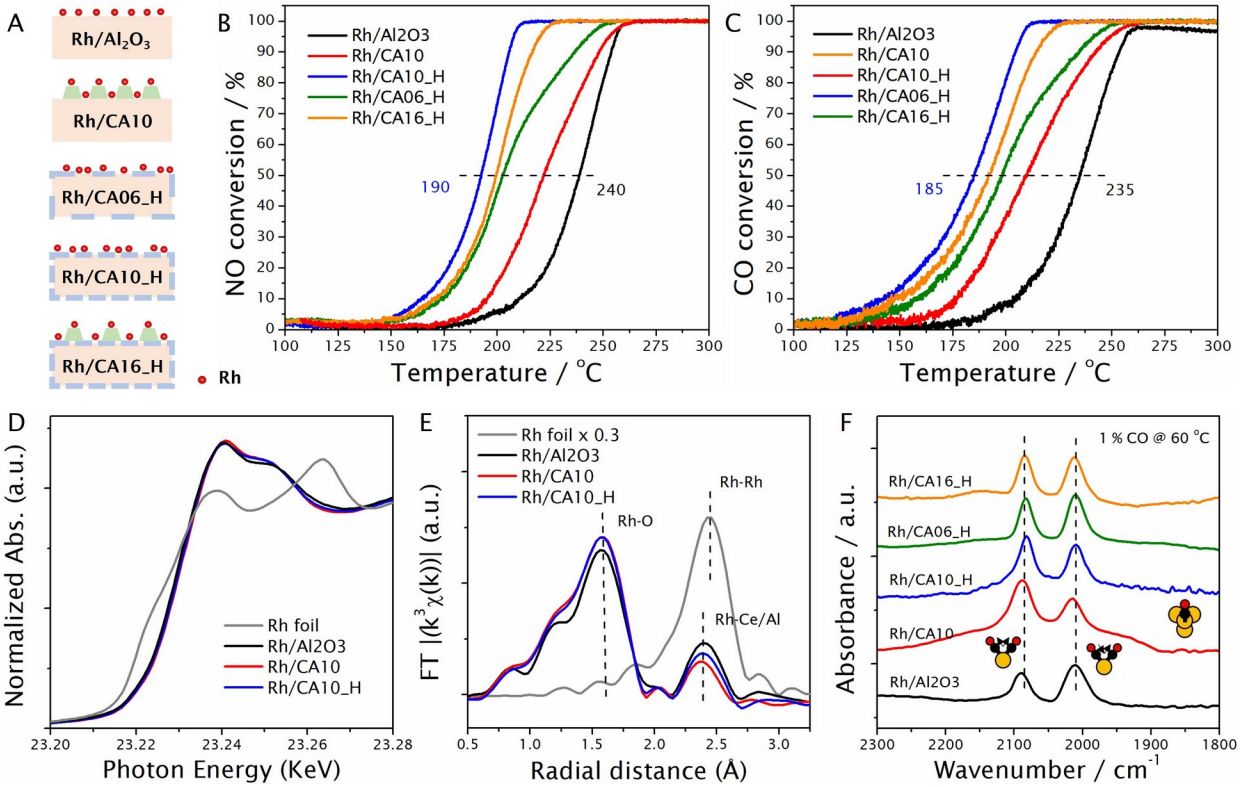

Fig. 2. Performance and spectroscopic characterization of Rh-based catalysts. (**A**) Schematic of Rh (0.1 wt %) on different supports, including Al_2O_3, CAx, CAx_H, and CeO_2. (**B**) – (**C**) Catalytic NO reduction by CO over different Rh catalysts under industrially relevant conditions. Reaction stream: 450 ppm NO, 2350 ppm CO, 950 ppm O_2, and 4.5 % H_2O, balanced with N_2. GHSV: 150 L g^{-1} h^{-1}. (**D**) Rh K-edge XANES spectra for Rh foil, Rh/Al_2O_3, Rh/CA10, and Rh/CA10_H. (**E**) Fourier transforms of k^3-weighted Rh K-edge EXAFS for Rh foil, Rh/Al_2O_3, Rh/CA10, and Rh/CA10_H. (**F**) CO-DRIFTS conducted at 60 ºC over different Rh catalysts. Spectra are collected after CO adsorption and helium purging.

Benefiting from the superior thermal stability of dispersed Ce_1 in air up to 500 ºC (Fig. 1A and fig. S8), CeO_x/Al_2O_3 (i.e., Ce_1 or CeO_2 on Al_2O_3) supported metal catalysts with well-defined hierarchical structures can be constructed. A small amount of Rh (0.1 wt %) was loaded on Al_2O_3 with controlled CeO_2 or Ce_1 coverage, where Rh was therefore associated with (neighbored by) bare Al_2O_3, crystalline CeO_2, or alternatively dispersed Ce_1 (Fig. 2A). The catalysts were tested for NO reduction by CO under industrially relevant conditions, in the presence of O_2 and H_2O and at a high space velocity (150 L g^{-1} h^{-1}), representative for testing automotive catalysts (*32*). For each catalyst, a second light-off curve was used as representative of its stable performance since as-synthesized catalysts (after air calcination) were tested under a stoichiometric condition (air/fuel ratio $\lambda = 1$), which could induce different surface states (fig. S9) (*33*). During the catalytic process, NO was mainly reduced by CO to N_2, with N_2O and NH_3 as by-products, while CO was oxidized to CO_2 by NO, O_2, and H_2O (fig. S10). As shown in Figs. 2B and 2C, Rh/CA10_H exhibited the best performance at low temperatures in converting both NO and CO. The T_{50} temperatures (required for 50 % NO/CO conversions) for Rh/CA10_H are 50 ºC lower than that for Rh/Al_2O_3.

To confirm the role of Rh in these catalysts, blank supports were also tested under the same condition, and were found to be totally inactive below 350 ºC and 250 ºC for converting NO and CO, respectively (fig. S11). Therefore, instead of bare Al_2O_3, crystalline CeO_2, or dispersed Ce_1, supported Rh are the intrinsic active centers in all catalysts. The influence of the support on the nature of loaded Rh was also studied, e.g., isolated Rh_1 cations versus Rh or Rh_2O_3 NPs (*34*). Synchrotron-based X-ray absorption spectroscopy (XAS) was used to study the chemical state and nuclearity of supported Rh. As shown in Fig. 2D, Rh exhibit almost identical X-ray absorption near edge structures (XANES) after being loaded on Al_2O_3, CA, and CA_H, distinctly different from that of the Rh foil, clearly indicating the formation of Rh cations in all catalysts (*35*). Extended X-ray absorption fine structure (EXAFS) analysis showed the dominance of Rh-O bond and absence of Rh-Rh bond in the catalysts (Fig. 2E) (*35*), suggesting the single-atom nature of supported Rh (i.e., Rh_1) in all studied catalysts (Fig. 2).

Diffuse reflectance infrared Fourier transform spectroscopy (DRIFTS) was conducted under flowing CO. All catalysts showed the exclusive presence of two peaks at ~ 2088 and 2015 cm^{-1} (Fig. 2F), which have been widely ascribed to the symmetric and asymmetric CO stretches from gem-dicarbonyl ($Rh_1(CO)_2$) complexes formed by CO adsorption on an isolated Rh_1 cation (*34*). Combined XAS and DRIFTS studies therefore confirmed that all catalysts contain mostly Rh_1 single atoms, although the coordination/electronic structures could be slightly different due to the varied Rh_1-support interactions, as indicated by slight difference in CO-IR frequency (Fig. 2F). These Rh_1 species are stable under rich NO-CO reaction conditions, as confirmed by DRIFTS of spent catalysts even after an *in-situ* CO reduction at 500 ºC (fig. S12). Given the negligible catalytic performance of supports as well as their limited impact on Rh speciation, the greatly enhanced NO-

CO reaction upon Ce_1 dispersion must come from changes in the local environment of active centers (Rh_1). Therefore, isolated Rh_1 neighbored by dispersed Ce_1 is much superior to Rh_1 coordinated with crystalline CeO_2 or bare Al_2O_3 in catalyzing NO reduction (Figs. 2A-2C).

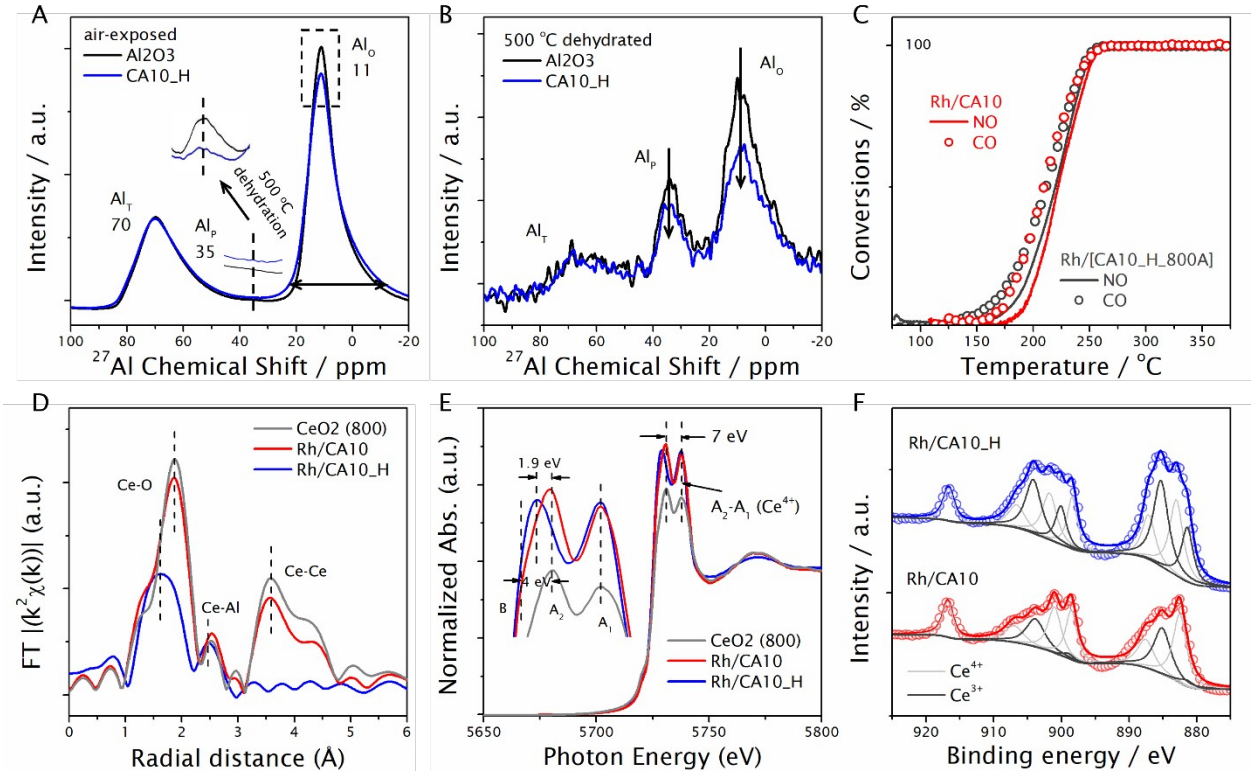

Fig. 3. Characterization and catalytic performance of Rh catalysts and supports. (**A**) Solid state ^{27}Al MAS NMR spectra of bare γ-Al_2O_3 and CA10_H in the air-exposed state. Insets show the evolution of Al_P peaks after dehydration at 500 °C. (**B**) ^{1}H–^{27}Al CP MAS NMR spectra of γ-Al_2O_3 and CA10_H after dehydration. Spectra were normalized by the same amount of γ-Al_2O_3. (**C**) NO-CO reaction over the Rh/CA10 and Rh/CA10_H_800A catalysts. (**D**) Normalized Ce L_{III}-edge XANES of 800 °C air-calcined CeO_2, Rh/CA10 and Rh/CA10_H. (**E**) Fourier transforms of Ce L_{III}-edge EXAFS spectra of 800 °C air-calcined CeO_2, Rh/CA10 and Rh/CA10_H. (**F**) Ce3d XPS spectra of Rh/CA10 and Rh/CA10_H.

To develop accurate structure-property relationships for the rational design of Ce_1-promoted catalysts, both the local structures of dispersed Ce_1 as well as its catalytic effects need to be unambiguously clarified. Strong interaction between Ce_1 and Al_2O_3 has been indicted by the outstanding thermal stability of dispersed Ce_1 (Fig. 1A), which is partially resistant to sintering even after 800 °C air calcination (fig. S13). In contrast, CeO_2 NPs are easily formed in the absence of such strong Ce_1-Al_2O_3 interaction (fig. S13). Solid-state magic angle spinning (MAS) ^{27}Al nuclear magnetic resonance (NMR) was used to investigate the structural modifications of γ-Al_2O_3. ^{27}Al MAS NMR spectra of Al_2O_3 and CA10_H in the air-exposed state showed two peaks at 11 and 70 ppm, ascribed to Al^{3+} in octahedral (Al_O) and tetrahedral (Al_T) coordination, respectively (Fig. 3A). Compared to Al_2O_3, CA10_H showed an Al_O peak with decreased intensity and broadened shoulders, indicating the coexistence of different Al_O sites, i.e., perturbed chemical environments of Al_O by dispersed Ce_1 (*36*). Such modifications were absent for CeO_2 NPs on Al_2O_3 (fig. S14). After dehydration, a pentahedral Al_P peak was observed in both supports at ~ 35 ppm (*37*), while a

small difference in Al_O is still discernible (fig. S15). The Al_P peak is much less pronounced in CA10_H, suggesting the consumption of Al_P as Ce_1 spreads over the Al_2O_3 surface (Fig. 3A). Therefore, both Al_P and Al_O sites contribute to stabilizing Ce_1.

^1H–^{27}Al cross-polarization (CP) MAS NMR that is highly surface sensitive was further used to probe Al close to surface hydroxyls (*38*). Both Al_P and Al_O peaks turned weaker with Ce_1 dispersion on Al_2O_3 surface (Fig. 3B), indicating that Ce_1 replaced hydroxyl near both sites, agreeing well with the statement above. Penta-Al^{3+} site has been proposed as the preferential nucleation site for different metals such like Ba, Pt, and Pd (*37, 39, 40*). Dispersed Ce_1 anchored by under-coordinated Al_P should show superior thermal stability to Ce_1-Al_O, consistent with the observation that < 1 wt % Ce_1 existed in as-calcined CA10 (fig. S3). More Ce_1-Al_P connections formed during Ce_1 dispersion, which survived after prolonged post-calcination (CA10_H_800A) (fig. S13). Rh/CA10_H_800A showed similar NO/CO conversions compared to Rh/CA10 (Fig. 3C), suggesting that Ce_1 strongly anchored by Al_P made limited contribution to the promoted NO reduction (Figs. 2B and 2C).

Synchrotron-based XAS was conducted to examine the chemical environments of dispersed Ce_1. As shown in the Ce L_{III}-edge EXAFS spectra, Rh/CA10 shows both intense Ce-O and Ce-Ce scatterings, similar to those of air-calcined CeO_2 (Fig. 3D). Interference from Rh is negligible due to the low loading (0.1 wt %). In contrast, Rh/CA10_H shows a shorter Ce-O bond (2.2 vs. 2.3 Å) with a coordination number of 7.26 ± 1.53 and a second Ce-Al shell (Ce-O-Al) at 3 Å (fig. S16 and table S1), confirming the exclusive presence of dispersed Ce_1 after Rh loading at 500 °C. The short Ce-O/Al distances explain the good thermal stability of dispersed Ce_1 (fig. S13). As shown in the Ce L_{III}-edge XANES spectra (Fig. 3E), both CeO_2 and Rh/CA10 show two prominent absorption peaks (A_1 and A_2) separated by 7 eV, transitions diagnostic of Ce^{4+}. In comparison, Rh/CA10_H shows a shifted A_2 feature towards lower energies by 1.9 eV. The characteristic B transition of Ce^{3+} is absent, which is ~ 4 eV lower than A_2 (*41*). This suggests that Rh/CA10_H contains a mixture of Ce^{3+} and Ce^{4+}, the latter still being the majority. The reduced Ce valency was also confirmed by X-ray photoelectron spectroscopy (XPS) that the Ce^{3+} content increased from ~ 31 % in Rh/CA10 to ~ 45 % in Rh/CA10_H (Fig. 3F). Besides Ce_1 dispersion, high-temperature reduction also induced surface electron enrichment as evidenced by the slightly lower Al2p and O1s energies in CA10_H (figs. S17 and S18).

With clarified Ce_1-Al_2O_3 surface structures, the catalytic effects of dispersed Ce_1 can now be discussed in detail. The promoting role of nanosized CeO_2 in heterogeneous catalysis originates from the facile oxygen transfer within the fluorite lattice, which has been generally evaluated by oxygen storage capacity (OSC) (*6*). OSC was measured over unsupported and Al_2O_3-supported CeO_2 (CA10), as well as dispersed Ce_1 on Al_2O_3 (CA10_H). Crystalline CeO_2 calcined at lower temperatures (500 vs. 800 °C) or supported on Al_2O_3 (CeO_2 vs. CA10) shows higher OSC values (Fig. 4A), which should be due to smaller particle size and rich defects. Surprisingly, although without structural integrity, dispersed Ce_1 on Al_2O_3 shows ~ 3-4 times higher OSC than crystalline CeO_2, approaching 2.1 mmol/g (CeO_2 basis) at 350 °C, 73 % of the theoretical maximum (Fig. 4A). The high OSC of CA10_H was maintained after 500 °C calcination (1.9 mmol/g) but drastically decreased (0.8 mmol/g) after 800 °C calcination (fig. S19). This is fully consistent with the structural evolution of Ce_1/CeO_2 upon controlled aging (Fig. 1A), confirming that the greatly enhanced OSC is associated with Ce_1 being dispersed on the Al_2O_3 surface.

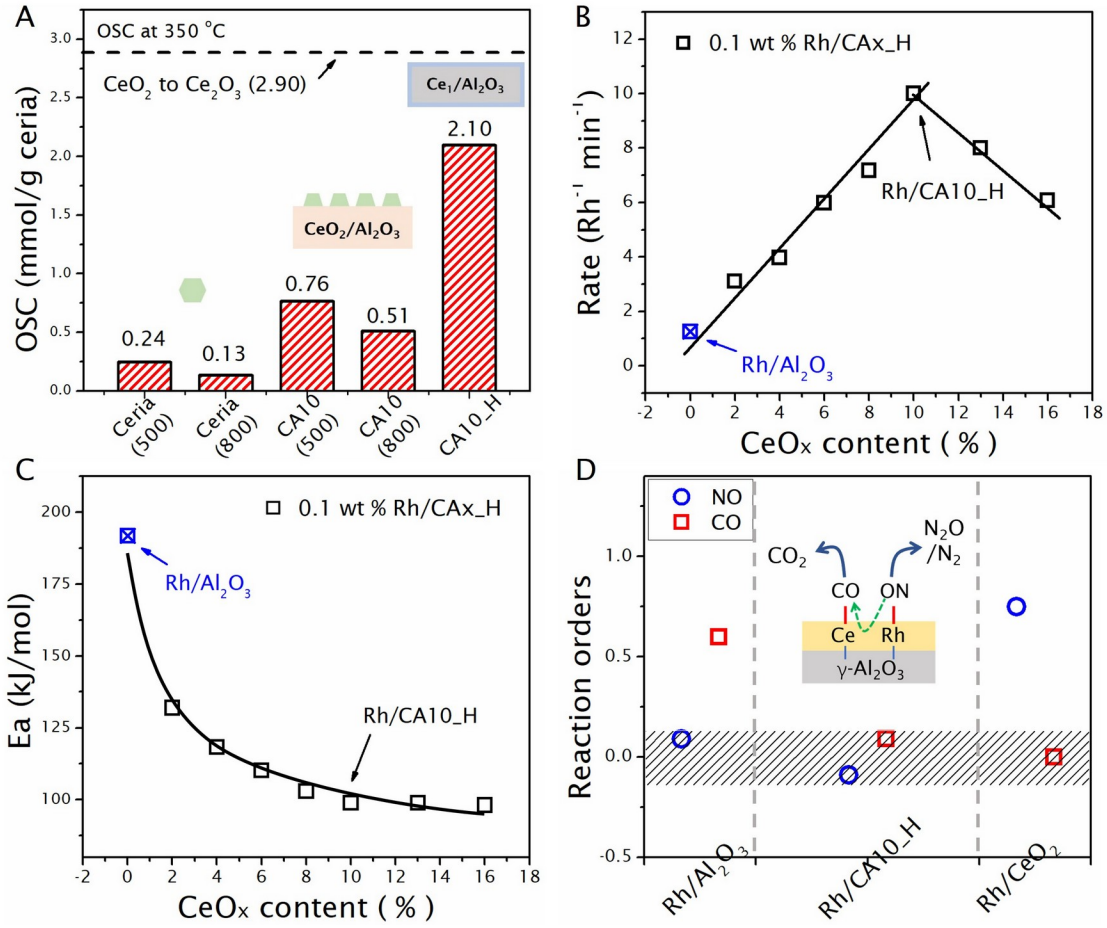

Fig. 4. Characterization and kinetic studies of Rh catalysts and supports. (**A**) oxygen storage capacity (OSC) measurements of CeO_2, CA10, and CA10_H. (**B**) Reaction rates of NO reduction over Rh/CAx_H (0 < x <16) measured at 250 °C under differential NO conversions, normalized by Rh_1. Conditions: 1000 ppm NO, 2000 ppm CO, N_2 balance. (**C**) Apparent activation energies (E_a) of Rh on Al_2O_3, CA10, and CAx_H (0 < x <16). Conditions: 1000 ppm NO, 2000 ppm CO, N_2 balance, 250-275 °C. (**D**) NO reduction rate dependence on partial pressures of NO (500-1400 ppm) and CO (1000-4000 ppm) at 260 °C. Inset is the proposed reaction scheme between activated NO and CO on neighbored Rh_1/Ce_1 single-atom pairs.

Such enhanced OSC of Ce_1/Al_2O_3 should benefit redox reaction on supported metal centers, e.g., Rh_1-catalyzed NO reduction which is mediated by oxygen transfer between NO and CO. Kinetic studies were conducted over Rh/CAx_H (0 < x < 16) to further understand the promoting role of dispersed Ce_1 in this reaction. As confirmed, up to 10 wt % CeO_2 can be fully dispersed into isolated Ce_1 after the high-temperature reductive treatment (i.e., CA10_H), beyond which crystalline CeO_2 formed (fig. S4). Notably, with increased amount of Ce_1 on Al_2O_3, the reaction rate of isolated Rh_1 at 250 °C increased linearly from 1.1 min^{-1} for Rh/Al_2O_3 to 10.1 min^{-1} for Rh/CA10_H, enhancement of almost one order of magnitude (Fig. 4B). This also indicates the absence of preferential nucleation of Rh since 2 wt % Ce_1 is sufficient to anchor 0.1 wt % Rh_1. Further increase of CeO_x (CeO_2 forms beyond 10 wt %) content resulted in decreased reaction rates (Fig. 4B). This is fully consistent with the light-off results (Fig. 2B), further confirming the high superiority of dispersed Ce_1 in promoting the Rh-catalyzed NO reduction.

Dispersed Ce_1 on Al_2O_3 greatly lowered the apparent activation energy (E_a) of NO reduction from 192 kJ/mol (Rh/Al_2O_3) to 96 kJ/mol (Rh/CA10_H), which kept almost constant with further increased CeO_x content (Fig. 4C and fig. S20). This clearly indicates that dispersed Ce_1 must have substantially modified the mechanism of Rh_1-catalyzed NO-CO reaction. Zhang et al. proposed the NO-CO reaction mechanism over isolated Rh_1 anchored by inert SiO_2 based on combined experimental and computational studies, the elementary step with the highest energy barrier being the coupling between activated NO* and CO* that are co-adsorbed on isolated Rh_1 (*42*). The calculated E_a (2.16 eV) is very close to the value we obtained over Rh/Al_2O_3 in the current work (Fig. 3C). Reaction rate dependence on the partial pressures of reactants ($P_{CO/NO}$) were measured over different Rh catalysts to shed light on the mechanism change upon Ce_1 dispersion (fig. S21). In contrast to Rh/Al_2O_3 which exhibited a positive order for CO (0.6) and a ~ 0 order for NO, and Rh/CeO_2 which exhibited a positive order for NO (0.75) and a ~ 0 order for CO, Rh/CA10_H exhibited ~ 0 orders for both NO and CO (Fig. 4D). Therefore, dispersed Ce_1 apparently facilitated the activation of reactants over neighboring Rh_1 centers.

Based on these OSC and kinetic measurements, a reaction model for the NO-CO reaction on isolated Rh_1 supported on Ce_1-modified γ-Al_2O_3 ($Rh_1/Ce_1/Al_2O_3$) is proposed, as indicated by the inset of Fig. 4D. In contrast to Rh/Al_2O_3 where NO and CO are adsorbed on one Rh_1 site, in the proposed model, NO and CO are adsorbed on isolated Rh_1 and neighboring Ce_1 cations anchored by Al_2O_3, respectively. The superior oxygen shuttling mediated by the atomically dispersed Ce_1 greatly promotes the reaction between the adsorbed Rh_1-NO* and Ce_1-CO* with a substantially decreased energy barrier, namely, greatly promoted redox cycles. As a result of the integrated enhancement in CO activation and NO*-CO* reaction that are both promoted by dispersed Ce_1, Rh_1 on Ce_1-modified γ-Al_2O_3 presents excellent NO reduction at low temperatures.

Recent interests in single-atom catalysis have been mostly focused on the effect of dispersing active metals. Here, we demonstrate that controlled dispersion of catalytic promoters which have been widely used in real catalysts can also substantially influence the activities of the integrated system. The understandings of reductive atom trapping of Ce_1 as well as its structure-property relationships obtained in this work could be implemented in the rational design of Ce_1-promoted catalysts for many other applications. Benefiting from the greatly enhanced OSC, we found that dispersed Ce_1 on Al_2O_3 is also effective in promoting the catalytic performance of supported Pt NPs (figs. S22 and S23) in the oxidation of CO and hydrocarbons (fig. S24). Use of colloidal Pt NPs help exclude the interference from difference in nuclearity and particle size. Besides, Ce_1 dispersion on Al_2O_3 results in other modified surface properties, including the formation of more weak acid sites (figs. S25 and S26) and the overall enhanced surface basicity (fig. S27). These observations could be further utilized to explore the field of acid-base catalysis.

References

1. C. Sun, H. Li, L. Chen, Nanostructured ceria-based materials: synthesis, properties, and applications. *Energy Environmental Science* **5**, 8475-8505 (2012).
2. D. Jiang *et al.*, Elucidation of the Active Sites in Single-Atom Pd1/CeO2 Catalysts for Low-Temperature CO Oxidation. *ACS Catalysis* **10**, 11356-11364 (2020).
3. Y. Li *et al.*, Dynamic structure of active sites in ceria-supported Pt catalysts for the water gas shift reaction. *Nature Communications* **12**, 914 (2021).

4. D. Jiang, W. Wang, S. Sun, L. Zhang, Y. Zheng, Equilibrating the Plasmonic and Catalytic Roles of Metallic Nanostructures in Photocatalytic Oxidation over Au-Modified CeO2. *ACS Catalysis* **5**, 613-621 (2015).
5. H. Sun *et al.*, Boosting Activity on Co4N Porous Nanosheet by Coupling CeO2 for Efficient Electrochemical Overall Water Splitting at High Current Densities. *Adv. Funct. Mater.* **30**, 1910596 (2020).
6. A. Trovarelli, Catalytic properties of ceria and CeO2-containing materials. *Catalysis Reviews* **38**, 439-520 (1996).
7. D. Jiang, W. Wang, L. Zhang, Y. Zheng, Z. Wang, Insights into the Surface-Defect Dependence of Photoreactivity over CeO2 Nanocrystals with Well-Defined Crystal Facets. *ACS Catalysis*, 4851-4858 (2015).
8. R. Si, M. Flytzani-Stephanopoulos, Shape and Crystal-Plane Effects of Nanoscale Ceria on the Activity of Au-CeO2 Catalysts for the Water–Gas Shift Reaction. *Angew. Chem. Int. Ed.* **47**, 2884-2887 (2008).
9. Z. Hu, H. Metiu, Effect of Dopants on the Energy of Oxygen-Vacancy Formation at the Surface of Ceria: Local or Global? *The Journal of Physical Chemistry C* **115**, 17898-17909 (2011).
10. R. Alcala *et al.*, Atomically Dispersed Dopants for Stabilizing Ceria Surface Area. *Applied Catalysis B: Environmental* **284**, 119722 (2021).
11. D. Jiang *et al.*, Tailoring the Local Environment of Platinum in Single-Atom Pt1/CeO2 Catalysts for Robust Low-Temperature CO Oxidation. *Angewandte Chemie International Edition* **60**, 26054-26062 (2021).
12. C. E. García-Vargas *et al.*, Activation of Lattice and Adatom Oxygen by Highly Stable Ceria-Supported Cu Single Atoms. *ACS Catalysis*, 13649-13662 (2022).
13. Q. An *et al.*, Cerium-Catalyzed C–H Functionalizations of Alkanes Utilizing Alcohols as Hydrogen Atom Transfer Agents. *Journal of the American Chemical Society* **142**, 6216-6226 (2020).
14. H. Tsurugi, K. Mashima, Renaissance of Homogeneous Cerium Catalysts with Unique Ce(IV/III) Couple: Redox-Mediated Organic Transformations Involving Homolysis of Ce(IV)–Ligand Covalent Bonds. *Journal of the American Chemical Society* **143**, 7879-7890 (2021).
15. B. Qiao *et al.*, Single-atom catalysis of CO oxidation using Pt1/FeOx. *Nature Chemistry* **3**, 634 (2011).
16. Y. Xia, M. Sayed, L. Zhang, B. Cheng, J. Yu, Single-atom heterogeneous photocatalysts. *Chem Catalysis*, (2021).
17. H. Xu, D. Cheng, D. Cao, X. C. Zeng, A universal principle for a rational design of single-atom electrocatalysts. *Nature Catalysis* **1**, 339-348 (2018).
18. F. Zaera, Designing Sites in Heterogeneous Catalysis: Are We Reaching Selectivities Competitive With Those of Homogeneous Catalysts? *Chemical Reviews*, (2022).
19. S. Hinokuma *et al.*, Subnano-particle Ce catalyst prepared by pulsed arc-plasma process. *Catalysis Communications* **54**, 81-85 (2014).
20. H. C. Kwon *et al.*, Catalytic Interplay of Ga, Pt, and Ce on the Alumina Surface Enabling High Activity, Selectivity, and Stability in Propane Dehydrogenation. *ACS Catalysis* **11**, 10767-10777 (2021).

21. K. A. Ledwa, L. Kepinski, M. Pawlyta, Atomically dispersed cerium species in NMxCe1-xO2/Al2O3 (NM=Rh, Ru) catalysts. *Materials Research Bulletin* **122**, 110673 (2020).
22. S. Luo *et al.*, Hierarchical Heterogeneity at the CeOx–TiO2 Interface: Electronic and Geometric Structural Influence on the Photocatalytic Activity of Oxide on Oxide Nanostructures. *The Journal of Physical Chemistry C* **119**, 2669-2679 (2015).
23. M. Yoo *et al.*, A tailored oxide interface creates dense Pt single-atom catalysts with high catalytic activity. *Energy & Environmental Science* **13**, 1231-1239 (2020).
24. H. N. Pham *et al.*, Designing Ceria/Alumina for Efficient Trapping of Platinum Single Atoms. *ACS Sustainable Chemistry & Engineering*, (2022).
25. K. Konstantin, Dramatic improvement of NO reduction activity via reversible re-dispersion of CeO2 nanoparticles into Ce+3 atoms on alumina under high temperature reactive treatment *ChemRxiv*, (2021).
26. H. Jeong *et al.*, Highly durable metal ensemble catalysts with full dispersion for automotive applications beyond single-atom catalysts. *Nature Catalysis*, (2020).
27. A. Martínez-Arias, J. M. Coronado, R. Cataluña, J. C. Conesa, J. Soria, Influence of Mutual Platinum-Dispersed Ceria Interactions on the Promoting Effect of Ceria for the CO Oxidation Reaction in a Pt/CeO2/Al2O3 Catalyst. *The Journal of Physical Chemistry B* **102**, 4357-4365 (1998).
28. W. Tan *et al.*, Highly efficient Pt catalyst on newly designed CeO2-ZrO2-Al2O3 support for catalytic removal of pollutants from vehicle exhaust. *Chemical Engineering Journal* **426**, 131855 (2021).
29. J. Shyu, W. Weber, H. Gandhi, Surface characterization of alumina-supported ceria. *The Journal of Physical Chemistry* **92**, 4964-4970 (1988).
30. M. Zhu *et al.*, Combining in-situ TEM observations and theoretical calculation for revealing the thermal stability of CeO2 nanoflowers. *Nano Research*, (2021).
31. M. A. Małecka, L. Kępiński, New, intermediate polymorph of CeAlO3 with hexagonal structure – formation and thermal stability. *CrystEngComm* **17**, 2273-2278 (2015).
32. K. G. Rappé *et al.*, Aftertreatment Protocols for Catalyst Characterization and Performance Evaluation: Low-Temperature Oxidation, Storage, Three-Way, and NH3-SCR Catalyst Test Protocols. *Emission Control Science and Technology* **5**, 183-214 (2019).
33. B. Zhao *et al.*, Insight into the effects of different ageing protocols on Rh/Al2O3 catalyst. *Applied Surface Science* **308**, 230-236 (2014).
34. C. Asokan, Y. Yang, A. Dang, A. B. Getsoian, P. Christopher, Low-Temperature Ammonia Production during NO Reduction by CO Is Due to Atomically Dispersed Rhodium Active Sites. *ACS Catalysis* **10**, 5217-5222 (2020).
35. M. Machida *et al.*, Catalyst Deactivation via Rhodium–Support Interactions under High-Temperature Oxidizing Conditions: A Comparative Study on Hexaaluminates versus Al2O3. *ACS Catalysis* **11**, 9462-9470 (2021).
36. C. Wan *et al.*, Investigating the Surface Structure of γ-Al2O3 Supported WOX Catalysts by High Field 27Al MAS NMR and Electronic Structure Calculations. *The Journal of Physical Chemistry C* **120**, 23093-23103 (2016).
37. J. H. Kwak *et al.*, Coordinatively Unsaturated Al3+ Centers as Binding Sites for Active Catalyst Phases of Platinum on g-Al2O3. *Science* **325**, 1670-1673 (2009).

38. A. T. F. Batista *et al.*, Beyond γ-Al2O3 crystallite surfaces: The hidden features of edges revealed by solid-state 1H NMR and DFT calculations. *Journal of Catalysis* **378**, 140-143 (2019).
39. H. Duan *et al.*, Pentacoordinated Al3+-Stabilized Active Pd Structures on Al2O3-Coated Palladium Catalysts for Methane Combustion. *Angewandte Chemie International Edition* **58**, 12043-12048 (2019).
40. J. H. Kwak, J. Z. Hu, D. H. Kim, J. Szanyi, C. H. F. Peden, Penta-coordinated Al3+ ions as preferential nucleation sites for BaO on γ-Al2O3: An ultra-high-magnetic field 27Al MAS NMR study. *Journal of Catalysis* **251**, 189-194 (2007).
41. R. G. Agarwal, H.-J. Kim, J. M. Mayer, Nanoparticle O–H Bond Dissociation Free Energies from Equilibrium Measurements of Cerium Oxide Colloids. *Journal of the American Chemical Society* **143**, 2896-2907 (2021).
42. S. Zhang *et al.*, Catalysis on Singly Dispersed Rh Atoms Anchored on an Inert Support. *ACS Catalysis* **8**, 110-121 (2018).

Acknowledgments:

This work was supported by the U.S. Department of Energy (DOE), Energy Efficiency and Renewable Energy (EERE), Vehicle Technologies Office (DE-FOA-0002197). Work at the Molecular Foundry was supported by the Office of Science, Office of Basic Energy Sciences, of the U.S. Department of Energy under Contract No. DE-AC02-05CH11231. This study used resources of the Advanced Photon Source, an Office of Science User Facility operated for the U.S. DOE Office of Science by Argonne National Laboratory and was supported by U.S. DOE under Contract DE-AC02-06CH11357, and the Canadian Light Source and its funding partners. Use of the Stanford Synchrotron Radiation Light source, SLAC National Accelerator Laboratory, is supported by the U.S. Department of Energy, Office of Science, Office of Basic Energy Sciences under Contract DE-AC02-76SF00515. The authors thank Dr. Angelica Benavidez at UNM for her help with part of XPS measurements.

Funding:

U.S. Department of Energy, DE-FOA-0002197

U.S. Department of Energy, DE-AC02-05CH11231

U.S. Department of Energy, DE-AC02-06CH11357

U.S. Department of Energy, DE-AC02-76SF00515

Competing interests: Authors declare no competing interests.

Data and materials availability: All data are available in the main text or the supplementary materials.

Supplementary Materials

Materials and Methods

Figs. S1 to S27

Tables S1

References (43-47)